

Earthquake-faulting-related deformation in soil evidenced in S-wave shallow reflection data: Field results from Portugal

Carvalho, João; Ghose, Ranajit; Alves, D.; Leote, J

DOI

[10.1190/GEO2015-0040.1](https://doi.org/10.1190/GEO2015-0040.1)

Publication date

2016

Document Version

Final published version

Published in

Geophysics

Citation (APA)

Carvalho, J., Ghose, R., Alves, D., & Leote, J. (2016). Earthquake-faulting-related deformation in soil evidenced in S-wave shallow reflection data: Field results from Portugal. *Geophysics*, 81(5), IM97-IM108. <https://doi.org/10.1190/GEO2015-0040.1>

Important note

To cite this publication, please use the final published version (if applicable). Please check the document version above.

Copyright

Other than for strictly personal use, it is not permitted to download, forward or distribute the text or part of it, without the consent of the author(s) and/or copyright holder(s), unless the work is under an open content license such as Creative Commons.

Takedown policy

Please contact us and provide details if you believe this document breaches copyrights. We will remove access to the work immediately and investigate your claim.

Earthquake-faulting-related deformation in soil evidenced in S-wave shallow reflection data: Field results from Portugal

João Carvalho¹, Ranajit Ghose², Daniela Alves³, and Jaime Leote¹

ABSTRACT

Expressions of ductile, soft-sediment deformations induced by ground movements due to past earthquakes are difficult to recognize in near-surface soils. We have carried out shallow S-wave reflection studies in a seismically active area located northeast of metropolitan Lisbon, Portugal. Identifying shallow disturbed zones and hidden fault segments in this area is important but quite difficult because of small vertical slips due to earthquakes, the Holocene alluvial cover hiding the fault segments, and a high rate of surficial sedimentation. We have performed S-wave reflection profiling at two sites — Vila Franca Xira and Castanheira de Ribatejo. We detected different but interrelated evidence of soft-sediment deformation in the seismic data. This evidence includes sharp lateral changes in the S-wave

velocity field; changes in the reflection horizons in stacked sections; aligned diffractions in unmigrated sections; discontinuities in common-offset gathers; and discontinuities, backscattered, and diffracted arrivals in common-source gathers. Though not equally clear everywhere, this evidence is recognizable at many locations where earthquake-motion-induced disturbed zones are interpreted. To confirm these interpretations, we have performed synthetic modeling of a seismic wavefield using the same acquisition geometry as in the field experiments, and with multiple disturbed zones present as vertical emplacements through horizontally lying soil layers. The modeling results resemble the observations in field data. It is possible to confirm the signatures of soft-sediment deformation in the shallow S-wave reflection data. The approach that we used will be useful in many seismically active, soil-covered areas in the world.

INTRODUCTION

In seismically active areas, the recognition and characterization of possible earthquake-faulting-related deformations hidden in the sediments or soil layers at shallow depths are important for many reasons. By exposing the upper few meters of soils across an active fault, paleoseismologists hope to find disturbed ancient soil layers or other traces left by past earthquakes. If we know the time of the last large earthquake and how often prehistoric earthquakes occur, then it is possible to estimate the probability of the next big earthquake. It is also known that the observed ground acceleration is strongly controlled by the distribution and composition of the shallow soil/sediment layers. An extremely thin layer of clay sediment below the ocean floor was the primary cause of the huge tsunami associated with the 2011 Tohoku earthquake (e.g., [Chester et al.](#),

[2013](#)). A thin layer of water-swelling clay in a fault zone can act as a lubricant during an earthquake slip. Small fault displacements produce general distortion of the soil, before larger displacements generate a shear localization at the base of a soil layer near the bedrock. The differential movement across a fault-rupture commonly dissipates as the rupture propagates toward the ground surface through unconsolidated earth materials, and the characteristics of the soil overlying the bedrock fault strongly influence the observed fault-rupture propagation behavior ([Bray et al., 1994](#)). It is, therefore, critical to be able to recognize and characterize the deformation zones in the shallow soil layers due to deeper earthquake-related faulting to relate the deformation to the local soil structure. Finally, identification of shallow-faulting-related deformation in sediments or soils is crucial also from hydrogeologic and engineering perspectives. A conceptual hydrogeologic model

Manuscript received by the Editor 25 January 2015; revised manuscript received 23 February 2016; published online 11 July 2016.

¹Laboratório Nacional de Energia e Geologia, Estrada da Portela, Bairro do Zambujal, Amadora, Portugal. E-mail: joao.carvalho@lneg.pt; jaime.leote@lneg.pt.

²Delft University of Technology, Department of Geoscience and Engineering, Delft, the Netherlands. E-mail: r.ghose@tudelft.nl.

³Formerly Laboratório Nacional de Energia e Geologia, Estrada da Portela, Bairro do Zambujal, Amadora, Portugal; presently Randstad, Lisboa, Portugal. E-mail: daniela.alves.planageo@ext.randstad.pt.

© 2016 Society of Exploration Geophysicists. All rights reserved.

of flow within a fault zone and surrounding area is essential to assess the potential for enhanced vertical connectivity between the shallow fractured zones/aquifers and the deeper ones.

There are two common approaches for investigating shallow faults: shallow trenching and geophysical exploration. Digging a trench across a fault and dating the soils disturbed by prior earthquakes is the best approach for investigating the history of earthquake faults. Although trenching and drilling offer direct ground truth, they cannot generally be carried out in urbanized or cultivated areas, and being invasive and localized in nature, they are usually performed when the location of a shallow fault is a priori anticipated based on other evidences. Seismic traveltime tomography or ground-penetrating radar (GPR) surveys are promising approaches to investigate shallow faults, provided the quality of data is high. In areas with soft sediments and a high water content and where the velocity contrast between the fault segments (containing material that has undergone ductile deformation) and the adjacent sediments is low, seismic tomographic inversion of traveltimes generally has insufficient resolution, given the frequency band and signal-to-noise ratio (S/N) typical of field seismic data. The GPR has depth-penetration problems in clayey environments with a shallow water table. Of the various geophysical methods, seismic reflections generally offer a good resolution to study the shallow fault zones (e.g., Woolery et al., 1993; Benson and Mustoe, 1995; Floyd et al., 2001; Williams et al., 2001; Sugiyama et al., 2003; Wang et al., 2004; Harris, 2009; Campbell et al., 2010). In case of soft soils, S-waves generally offer better results than P-waves not only because of the higher resolution due to much lower velocity and hence smaller wavelengths, but also owing to a greater sensitivity of S-waves to the subtle changes in the soil

type or composition (e.g., Brouwer et al., 1997; Ghose and Goudswaard, 2004; Ghose, 2012). The vast majority of previous studies involving shallow seismic reflections to illuminate a fault zone relied on detecting a displacement in one or more reflection horizons due to faulting, generally observed in the stacked section. Such clear discontinuity in a reflection horizon is discernible only when the faulting-related displacement of a layer boundary is significant with respect to seismic wavelength. This is, however, often not the case.

Identification of faulting-related soft-sediment deformation in the shallow seismic reflection data is generally a challenging task. This is because the faulting-related displacement of a soil-layer boundary is often quite small compared to the seismic wavelength, or the shallow fault zone is steeply dipping, or the background noise in the data is high, or a combination of these factors. In such cases, the evidence of deformation can be mistaken as a change in the very shallow region, a lateral change in geology, or a velocity anomaly. More importantly, the faulting-related deformation in soft (Holocene) sediments differs greatly from the brittle deformation in more compacted soils or hard rocks. Brittle deformation produces a steplike displacement of a layer boundary. Ductile soft-sediment deformations, on the other hand, result in grain reorganization, disaggregation bands, intrusion of liquefied sand along weak zones, water escape structures, slumping, steplike undulation of a layer boundary due to synsedimentary faulting, mixing of material in shear zone, and wedgelike penetration of material with a different hydromechanical property (e.g., Vanneste et al., 1999; Neuwerth et al., 2006; van Loon, 2009; Fossen, 2010; Alsop and Marco, 2011; Suter et al., 2011). Figure 1 illustrates a few examples of these types of deformations.

As part of a large project, we had the opportunity to carry out a detailed search using high-resolution seismic reflection surveys in a seismically active area located northeast of the metropolitan Lisbon, Portugal. Identifying shallow faults in this area is especially difficult due to small vertical slips due to earthquakes, Holocene alluvial cover hiding many fault segments, and high rate of surficial erosion. A shallow water table and a lack of geologic markers limit the success of investigation based on trenching alone. The focus of our research was on recognizing the evidences of seismogenic soft-sediment deformation hidden in the very shallow soil layers of the Lower Tagus Valley region, using shallow S-wave reflections. The tectonic deformation in this area is accommodated by displacements along numerous separate fault segments. Because of the proximity of a large metropolitan area and the past history of major catastrophic earthquakes in the region, the outcome of this study is important to seismologists and earthquake engineers. Ghose et al. (2013) present new evidences of deformation at one single fault segment at a given location. In this paper, we present detailed results on several fault segments at two different sites, showing multiple signatures of ductile, soft-sediment deformation associated with earthquake faulting. The observation is corroborated by the results of synthetic modeling. Through a systematic integration of multiple evidences of faulting-related deformation in soft sediments, we propose an approach that leads to increased confidence in the identification of disturbed zones and the associated changes in the shallow subsoil.

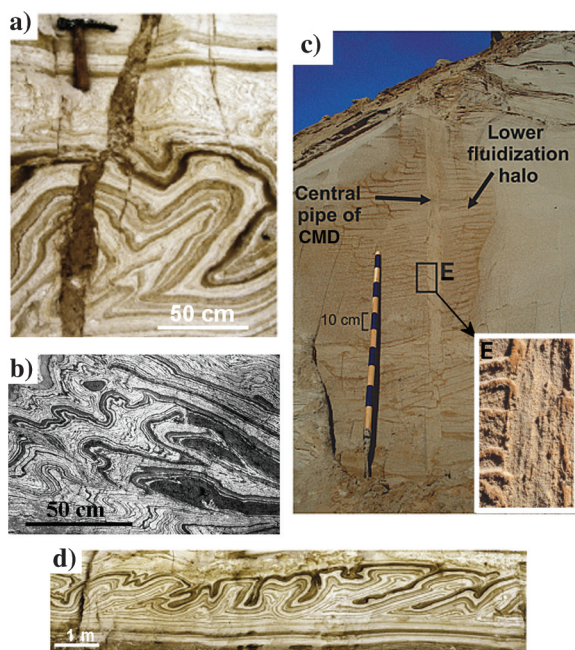


Figure 1. Examples of typical seismogenic ductile deformation in soft sediments: (a) vertical intrusion of liquefied material (Alsop and Marco, 2011), (b) folds in a slump structure (van Loon, 2009), (c) clastic megadike with a distinct central pipe and pipe halo (after Pisarska-Jamro and Weckwerth, 2013), and (d) step like folding (Alsop and Marco, 2011).

GEOLOGIC SETTING AND PREVIOUS WORK

Mainland Portugal is located approximately 200 km north of the Africa-Iberia plate boundary (Figure 2a). Portugal experiences occasionally destructive earthquakes, originated not only at this plate boundary but also at local intraplate faults. These local faults have

low slip rates like the faults in southeastern Spain, in Rhine graben, or in Mongolia (e.g., Perea et al., 2003; Ferry et al., 2005). They can produce moderate to large earthquakes, causing major damage and loss of lives. The destructive earthquakes in this region recur at an approximate interval of 200 years (Cabral et al., 2003; Carvalho et al., 2006). The shallow fault segments and disturbed zones are difficult to identify in the Holocene sediments because the small scarps generated by these earthquakes are easily erased by the surface processes during the long return period.

Figure 2b shows the location of the Vila Franca de Xira (VFX) fault. Our study area is marked. The area is located close to the city of Vila Franca de Xira, which is only 25 km northeast of the densely populated metropolitan Lisbon. The VFX fault is thought to have been active through the Holocene and responsible for several damaging earthquakes that affected the city of Lisbon and neighboring cities, such as in 1344 (e.g., Cabral et al., 2003), 1531 (Justo and Salwa, 1998), 1807 (Bensaúde et al., 2011), and 1909 (Cabral et al., 2013). The disastrous 1531 (MM VIII-IX) Lisbon earthquake caused more than 1000 fatalities (Justo and Salwa, 1998).

In a nearly 20 km long outcrop, the VFX fault expresses in the field as an east-verging reverse fault. The fault affects the upper Miocene (Tortonian) and older deposits; earlier seismic data suggest that the slip on the fault continued to even younger deposits (Cabral et al., 2003). No direct evidence of faulting was, however, detected in the post-Miocene sediments that outcrop on the eastern side of the fault zone.

The VFX fault zone has clear expressions in the potential field data (Carvalho et al., 2008, 2011) and oil-industry P-wave seismic reflection data (Rasmussen et al., 1998; Carvalho et al., 2005). Several fault segments at depths beyond 40 m were interpreted based on P-wave seismic reflection and borehole data (Carvalho et al., 2006). However, the limited resolution in the P-wave reflection data in the top 40 m made it impossible to identify any faulting-related feature in the Holocene sediments. This led to the acquisition in 2009 of an S-wave seismic reflection data set at the same location (Ghose et al., 2013). This study revealed for the first time that the VFX fault affected the alluvial deposits at a depth as shallow as 10 m.

From boreholes that were earlier drilled in this area, it is known that the top 1.5 m of man-made soil cover is underlain by a low-strength, black, muddy layer, which goes down to 8–10 m depth. From this depth till approximately 22–25 m, it is silty mud. Beyond that, the soil becomes more sandy, finally reaching a clayey sandstone layer below 30 m. The presence of faulting in the Holocene sediments could not be inferred from the sparse drilling data and typical alluvial depositional patterns.

FIELD MEASUREMENTS AND DATA PROCESSING: HIGH-RESOLUTION S-WAVE REFLECTION

S-wave reflection data were acquired at two sites: VFX and Castanheira do Ribatejo (CDR). The two sites are separated by approximately 2 km and are located in the alluvial plane, approximately 0.5 km east of an exposed fault scarp (see Figure 2b). The goal was to look for multiple fault segments and disturbed zones in the shallowest part of the VFX fault zone beneath the Holocene alluvial cover. S-wave reflection data acquisition involved a sledge-hammer source made of a wooden plank approximately 2.5 m long and oriented in the crossline (SH) direction and pressed by the wheels of a

jeep. Walk-away noise tests were performed first to optimize the acquisition parameters and ensure no spatial and temporal aliasing. The data were sampled at 1 kHz Nyquist frequency (0.5 ms time sampling). The recorded trace length was 1 s. An inline end-on acquisition geometry was used to acquire the data. Forty-eight horizontal geophones were planted at 0.75 m spacing. The vertical (source) stack count was four. The minimum source-receiver offset was 4 m. The source and receivers were moved each time by one receiver spacing. To avoid artifacts due to varying common midpoint (CMP) fold across the line, 36 geophone channels in end-on geometry were used in generating the stacked section, resulting in a constant CMP fold of 18. We also generated the stacked section using 48-channel shot gathers to look for any significant improvement, but the difference was small.

At VFX, the orientation of the seismic line was chosen such that the line crossed an anticipated fault segment in the middle (based on available P-wave data of Carvalho et al., 2006). The location for the profile at the second site (CDR) was selected by drawing an extension of a nearby fault outcrop and taking into consideration earlier fault interpretation at the VFX site.

The surface condition at both sites was very dry. The water table depth was approximately 2 m at both sites. At VFX, the profile was located on a compacted embankment of approximately 2 m thickness, whereas at CDR, the line was shot on a less-compacted pedestrian path made of local soils. The dry and compacted embankment at VFX site has been helpful in producing relatively high-

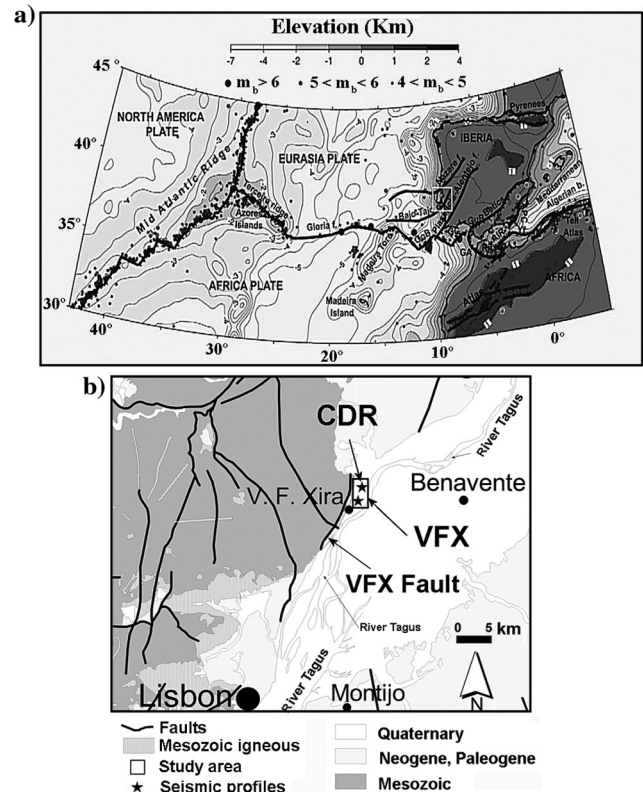


Figure 2. (a) Seismotectonic setting of Portugal along with the distribution of earthquakes and the study area (white-bordered rectangle) (after Jiménez-Munt and Negro, 2003). (b) Simplified geology, the locations of the study area, the VFX fault and VFX and CDR shear-wave seismic profile locations.

frequency shear waves and negligible surface (Love) waves. At CDR, the surface waves are prominent. To prevent weakening or losing any signature of shallow faulting in the data, the data processing was restricted to the minimum essential steps. The processing flow was nearly the same for the two data sets and involved geometry installation, vertical stacking, trace editing, first-arrival muting, gain correction, spectral whitening (30–90 Hz), band-pass filtering (25–120 Hz), velocity analysis, residual static correction, again velocity analysis, and CMP stacking.

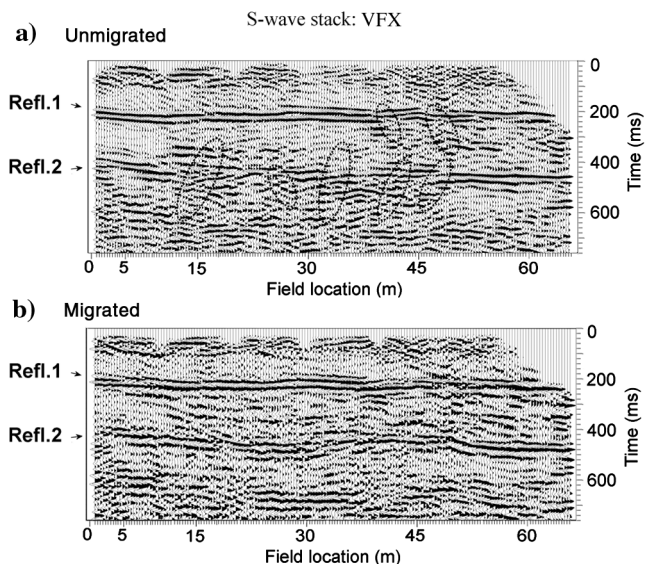


Figure 3. Unmigrated (a) and migrated (b) S-wave stacked section at VFX. The main reflection horizons (Refl.1 and Refl.2) in this area are verified in independent borehole measurements. Dotted ellipses in the unmigrated section mark regions with aligned diffractions.

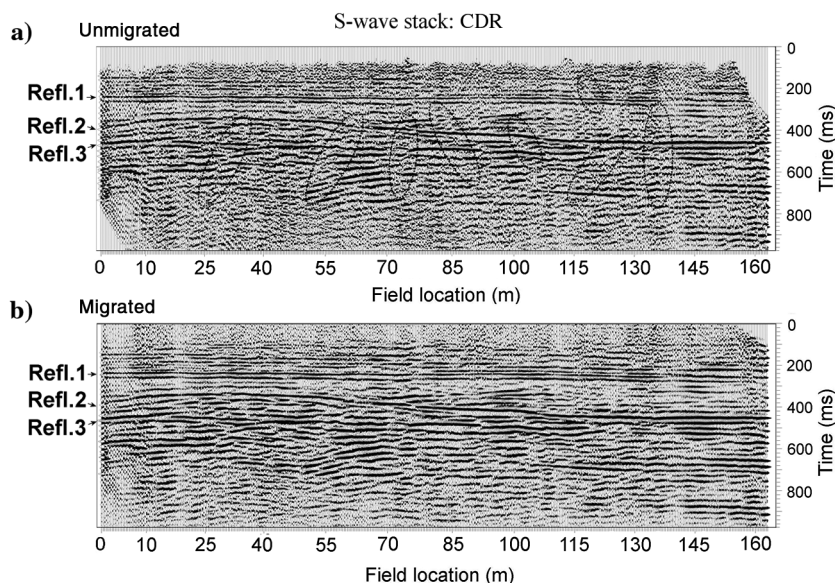


Figure 4. Unmigrated (a) and migrated (b) S-wave stacked section at CDR. The main reflection horizons (Refl.1, Refl.2, and Refl.3) in this area are verified in independent borehole measurements. Dotted ellipses in the unmigrated section mark regions with aligned diffractions.

The CDR data set is much noisier than the VFX data set due to ongoing agricultural and transportation activities in the field during the acquisition of seismic data. To remove surface waves in the CDR data set, early muting and a smooth dip filter were applied. Care was taken to ensure that the dip filter did not introduce any artifacts. Finally, a prestack time migration (PSTM) using a Kirchhoff algorithm was carried out for the VFX data set, and PSTM was preferred to poststack migration due to conflicting moveouts of the reflection hyperbolae in this data set. For the CDR data, FK DMO (Hale, 1984) was followed by the poststack migration (Stolt, 1978). To stack the data, we used a velocity function obtained from horizon velocity analysis (see the subsection “Local changes in rms velocity from automatic HOVA”) and constant velocity stacks. The S-wave stacked sections for the VFX and CDR sites are shown in Figures 3 and 4, respectively. Note the high resolution in the stacked images that has been achieved through the use of S-waves. The S-wave velocity (V_S) in the alluvial soil layers generally varies between 80 and 120 m/s. The predominant frequency in the data is in 50–80 Hz frequency range, resulting generally in a wavelength of 1–2 m and a resolution of 0.5 m or finer. The high-resolution details in the seismic data, in addition to the intrinsic sensitivity of S-waves to subtle changes in soil type (e.g., Ghose, 2003; Ghose and Goudswaard, 2004), are useful in detecting changes in soil due to faulting-induced soft sediment deformation.

FAULTING-RELATED DEFORMATION IN SOIL: SYNTHESIS OF MULTIPLE SIGNATURES IN S-WAVE REFLECTIONS

As remarked earlier, when the displacement of a layer boundary due to seismogenic faulting is a significant fraction or multiple of the seismic wavelength, it is straightforward to interpret that on the stacked seismic reflection section. However, quite often that is not the case, especially in case of deformation in near-surface soils due to earthquake-induced ground shaking. Additionally, in case of ductile deformation of soft sediments, there is generally no sharp (brittle) displacement of a layer boundary. On the contrary, the local flow paths of the liquefied material dominate the deformation pattern (Figure 1). To recognize/interpret such changes in soil on high-resolution seismic reflection data, a preferred approach will be to search for multiple signatures of such changes in the observed seismic wavefield. In case several independently extracted features point to the occurrence of faulting-related deformation in soil, then that enhances the confidence of interpretation.

In our study, we have found the following six evidences of soft-sediment deformation in the S-wave reflection data at each field location where the presence of such disturbances are suspected: (1) local changes in the V_S determined by horizon-consistent velocity analysis (HOVA) of primary reflection events, (2) structural changes/disturbances in the reflection horizons in the stacked section, (3) aligned diffractions in the unmigrated stacked sections, (4) discontinuity or undulation in common-offset gathers (COGs),

(5) discontinuity or undulation in reflection moveout in COGs, and (6) backscattered and diffracted energy from the disturbed zone. All of these six evidences do not manifest clearly at every location. Although some of these evidences are interrelated, their simultaneous presence at a given location is confirmatory. Some causes may contribute to all of these features, whereas others contribute to a part of them. For a reliable interpretation, it is necessary to carry out forward modeling of seismic wave propagation mimicking the field acquisition geometry and earthquake-induced, multiple disturbed zones in soil. Next, we look at these evidences in the VFX and CDR data sets.

Local changes in rms velocity from automatic HOVA

It is shown earlier that subtle changes in the subsoil may not be recognizable in S-wave stacked section, but they may be manifested in the V_S field (Ghose and Goudswaard, 2004). Therefore, we examine carefully the lateral variation in V_S along a reflection horizon. We select the prominent, laterally continuous reflection horizons at sites VFX and CDR. At VFX, there are two distinct reflectors (Refl.1 and Refl.2 in Figure 3) present at approximately 200 and 420 ms two-way times, respectively, whereas at CDR, there is an additional strong reflector with a two-way time approximately 500 ms (Refl.3 in Figure 4) — distinct between 0 and 120 m field locations. According to nearby well data, the 200 ms reflection horizon corresponds to a low-strength sand to silty-mud boundary at approximately 10 m depth and the 420 ms event corresponds to a silty-mud to dense-sand boundary at 22–25 m. The 500-ms event is probably the base of the alluvium, as found in borehole data. The two-way (normal moveout) time of these main reflection events are picked by digital search of the peak amplitude within a given time window (TW) for every trace (CMP location) in the stacked sections (Figures 3 and 4). These picked horizon times are indicated by red lines in Figures 5a and 6a for the VFX and CDR sites, respectively. Next, a TW around the automatically picked peak amplitude at each of these horizons is chosen. The semblance value for the chosen reflection event in each CMP gather is then estimated for all possible stacking velocities, assuming a flat reflector. In case of our data, the dip of the layers is rather small (even considering the dipping horizon Refl.2 at CDR), and therefore, the effect of data smearing is small.

Figure 5b shows the result of HOVA for reflection horizon Refl.1 (two-way time approximately 200 ms) at the VFX site. True and relative (scaled to the maximum amplitude in a trace) amplitudes were calculated, and different TW were used. The results were little affected as the TW lengths varied, indicating estimation stability. When the maximum offset in the CMP gather was altered, the result remained stable. The value of the estimated semblance is shown in color in which deep blue corresponds to the highest semblance. Figure 5c shows the results for horizon Refl.2 (two-way time approximately 420 ms event) at VFX also for a TW of 50 ms. We notice that there are distinct steplike changes (marked by arrows in Figure 5b and 5c) in the maximum semblance velocity at several locations along horizons

Refl.1 and Refl.2 at VFX. Arrows indicate locations where the velocity change is larger than 10 m/s. These V_S changes have been shown only inside the constant fold part of the profile (bounded by vertical dashed lines in Figure 5b and 5c). Most of these velocity changes are located in areas that spatially coincide with the location of disturbances observed in the stacked sections (see the subsection

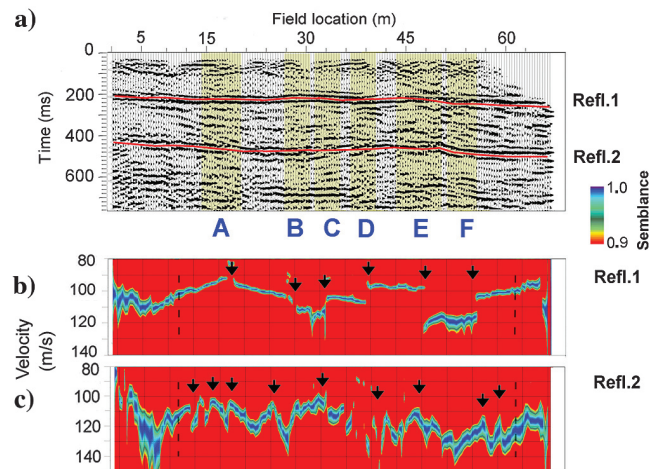


Figure 5. Result of HOVA at the VFX site: (a) automatic horizon picks (red lines) for Refl.1 and Refl.2, (b) result of HOVA for Refl.1 with TW length of 50 ms, (c) result of HOVA for Refl.2 with TW 50 ms. Locations showing steplike changes in the rms velocity by at least 10 m/s and which are located inside the constant CMP-fold part of the profile (dashed vertical lines in [b] and [c]) are marked by arrows. Letters A to F indicate locations where there are generally disturbances in the main reflection horizons in the stacked section (see yellow-shaded areas in [a] and in Figure 3).

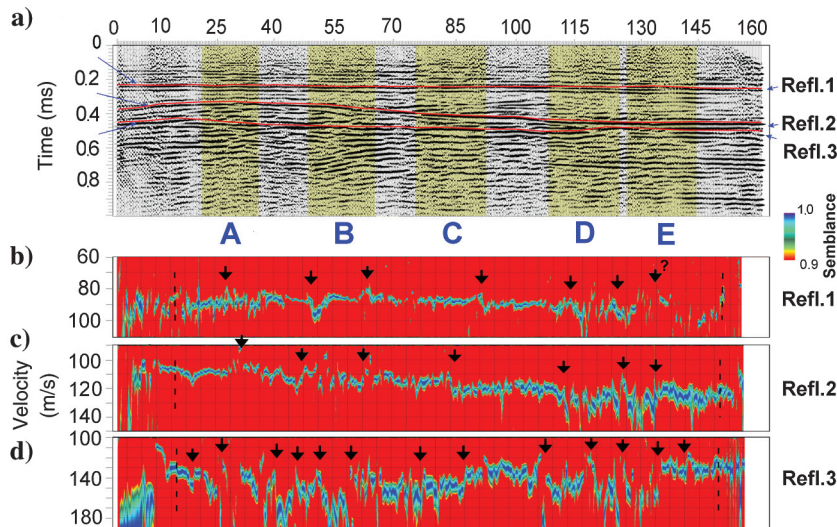


Figure 6. Result of HOVA at the CDR site: (a) automatic horizon picks (red lines) for Refl.1, Refl.2, and Refl.3, (b) result of HOVA for Refl.1 with TW 70 ms, (c) result of HOVA for Refl. 2 with TW 70 ms, (d) result of HOVA for Refl. 3 with TW 70 ms. Areas showing steplike changes in the rms velocity, which are not less than 10 m/s and which are located inside the constant CMP-fold part of the profile (dashed vertical lines) are marked by arrows. Letters A to E indicate these locations, where there are also generally disturbances in the main reflection horizons in the stacked section (yellow-shaded areas in [a] and in Figure 4).

“Disturbances in the main reflection horizons in stacked section”) and have been highlighted by yellow bands and letters A to F in Figure 5a. These steplike lateral changes in the root-mean-square (rms) velocity are more conspicuous for horizon Refl.1 than for horizon Refl.2. The magnitude (value of semblance) of these velocity changes is indicative of the clarity/strength of the estimate. Because the entire analysis is done automatically, it is necessary to keep the range of the displayed semblance narrow, to reduce the effect of noise present in the data.

Figure 6b–6d shows similarly the results of HOVA for reflection horizons Refl.1, Refl.2, and Refl.3, respectively, for the CDR site. Here, the semblance values for TW length of 70 ms are shown in color. True amplitudes are used. Lateral changes in the estimated rms velocity larger than 10 m/s along the chosen horizons are apparent at several locations (marked by arrows in Figure 6b and 6c); however, they are not as clear as in the VFX site.

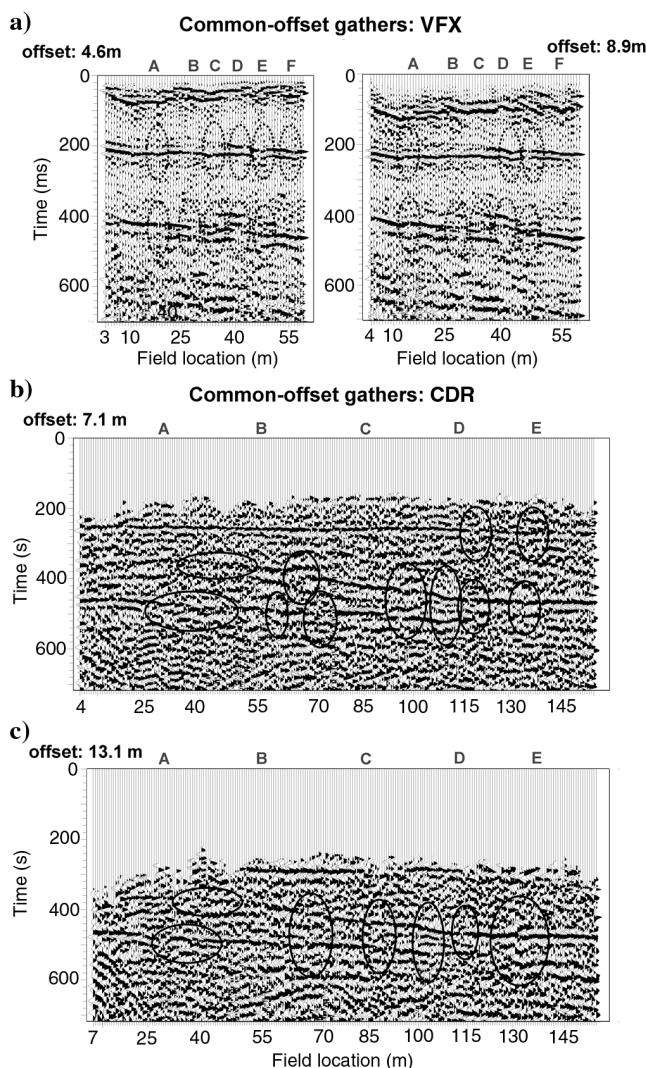


Figure 7. Typical COG for (a) VFX, (b) CDR S-wave reflection data sets. Common source-receiver offsets are marked. Presence of discontinuities and disturbances in the main reflections horizons is marked by dotted ellipses. Letters A to F show the field locations where steplike changes were detected in HOVA (Figures 5 and 6).

Disturbances in the main reflection horizons in stacked section

Next, we revisit the stacked section at VFX (Figure 3) and examine the locations, which correspond to those of the lateral changes observed in the rms velocity from HOVA (yellow-shaded areas A to F in Figure 5a). Interestingly, we recognize disturbances/discontinuities along reflection horizon Refl.2 and less clear ones along horizon Refl.1. The structural disturbances along Refl.2 appear as fault segmentations. It is likely that in the shallower region (till horizon Refl.1), which is made of low-strength muds, the earthquake faulting-related deformation causes typical soft-sediment deformation dominated by fluid flow and liquefaction, and no sharp displacements of the layer boundary. This is possibly the reason why we observe for Refl.1 lateral changes in the rms velocity (Figure 5b and 5c) but little displacement in the layer boundary as seen in the stacked section. At depths below horizon Refl.1, the soil becomes silty and the soft-sediment deformation pattern is less conspicuous. We indeed notice more structural disturbances in Refl.2 (Figures 3a and 4a), but less-conspicuous lateral changes in the rms velocity (Figure 5c).

Similar search is made on the S-wave reflection section at site CDR (Figure 4). At locations A to E (Figure 6b–6d), in which we notice apparent changes in HOVA rms velocity, we also distinguish discontinuities in the main reflection horizons — Refl.1, Refl.2, and Refl.3 (Figures 4 and 6a). The lateral disturbances in the stacked horizon are clearer for Refl.2 than for Refl.1, similar to the VFX site. For horizon Refl.3, the discontinuities are unclear. Note that, similar to the VFX data set, the changes in the rms velocity from HOVA are clearer for horizon Refl.1 than for Refl.2 and Refl.3, which possibly implies a more substantial soft-sediment deformation at the shallow depths consisting of soft mud, than at the deeper, more compacted, silty layers.

Diffractions in the unmigrated stacked sections

Figures 3a, 4a and 3b, 4b show, respectively, the unmigrated and migrated stacked sections for the VFX and CDR sites, respectively. Unlike in the migrated section (Figures 3b and 4b), the unmigrated sections (Figures 3a and 4a) suggest the presence of aligned diffracted energy and disruptions. These have been marked by dotted ellipses. Such alignment of diffractions is more distinct at the VFX site than at the CDR site. Note that the locations of these identified zones of aligned seismic diffractions in the stacked section generally coincide with the location of the observed steplike changes in the lateral distribution of the rms velocity along the primary reflectors as estimated by HOVA (Figures 5 and 6).

Discontinuity in COG

Figure 7a and 7b shows COG for the VFX and CDR sites, respectively. A careful look at the VFX gathers reveals consistent discontinuities (undulations, breaks, amplitude changes) in the primary reflections at several locations (marked by dashed ellipses), which generally coincide with the locations of anomalies detected in HOVA (Figures 5 and 6) and stacked sections (Figures 3 and 4).

Discontinuity in reflection moveout in shot gathers

Next, we examine the moveout of the primary reflection events in the shot gathers. Figure 8a shows four typical raw shot gathers from

the VFX site. Note the clear discontinuities in the reflections moveouts, marked by dashed-line arrows. Interestingly, the location of a seismogenic-faulting-related disturbed zone as interpreted in Figures 5 and 6 is about halfway between the source location and the receiver location corresponding to the discontinuity. As noticed earlier, the discontinuities are more conspicuous for the reflection event corresponding to Refl.2 than that corresponding to the shallower horizon Refl.1. Figure 8b shows similar results in representative shot gathers from the CDR site. Here, the discontinuities are less prominent due to a much lower S/N.

Backscattered and diffracted arrivals in shot gathers

A careful look at the shot gathers shown in Figure 8a and 8b reveals also the presence of backscattered energy (marked by continuous-line arrows), with negative velocity in the space-time domain. Such backscattered energy might appear if subvertical fault segments or disturbed zones are present in the subsol. Also, diffractions resulting from abrupt layer terminations against the fault segments and from the internal structures of the fault are expected because the anticipated structural variations are of the order of the seismic wavelength. Such backscattered and diffracted arrivals are visible in many shot gathers. They are more easily identifiable at VFX than at CDR because of more noise in the latter data set. This backscattered/diffracted energy is more noticeable at larger times (below 400 ms at both sites). This is possibly due to greater displacements across the fault segments at greater depths. An interpretation of such events, however, requires forward modeling of the seismic wavefield.

FORWARD MODELING OF S-WAVE REFLECTION DATA CONSIDERING MULTIPLE DISTURBED ZONES PRESENT IN SOIL

Forward modeling has been performed using the same acquisition parameters as in field experiments. In forward modeling, for simplicity, at first one single disturbed zone is embedded vertically in a four-layered model. S-wave velocity is assigned based on interval velocity estimated from the stacking velocities. The disturbed zone has a limited (1.5 m) lateral extent, the V_S in this zone is 10%–20% less than the background layers, in agreement with the velocity changes observed in the result of HOVA (Figures 5 and 6). The narrow disturbed zone extends from the surface to 30 m depth (Figure 9a). Note that there is no vertical displacement in the layer boundaries across the disturbed zone. This is to mimic the local emplacement in soil of a fluidized, low-velocity soil material, representing typical seismogenic soft-sediment deformation. As in field experiments, 48 geophones are positioned along a line, with 75 cm spacing between geophones. A Ricker wavelet of 40 Hz center frequency is used as the source wavelet, as this resulted in a maximum frequency of 110 Hz and the frequency content in the field data ranging between 30 and

90 Hz, although much of the signal energy was in 50–80 Hz range. The synthetic shot gather for a crossline shear source is calculated using an elastic finite-difference code (Thorbecke and Draganov, 2011). The four-layered model is constructed based on borehole information and the known stratigraphy of the Holocene alluvium in this area (Vis and Kasse, 2009).

Figure 9a and 9b illustrates schematically, for the four-layered model containing a vertical disturbed zone, the ray paths for reflected, and backscattered seismic events, respectively. Figure 9c shows the synthetic shot gather for the four-layered model when there is no disturbed zone. The direct wave is marked as dw and the surface wave train as sw . The primary reflections are marked as $a1$, $a2$, and $a3$. A multiple reflection inside the third layer (velocity of 135 m/s) has also been identified ($a4$). Figure 9d shows the synthetic shot gather when a vertical fault segment or a disturbed zone is present. The location of the fault segment is marked (arrow) on the upper margin of Figure 9d. Note the arrival of backscattered events — $b1$, $b2$, and $b3$, etc., which are remarkably similar to what we notice in the observed shot gathers in field at VFX and CDR sites (Figure 8a and 8b). We can also notice that in Figure 9c (shot gather with no fault segment present) that there are slight undulations in the moveout of the reflection events. However, these are smaller than the undulations visible in Figure 9d. The small ampli-

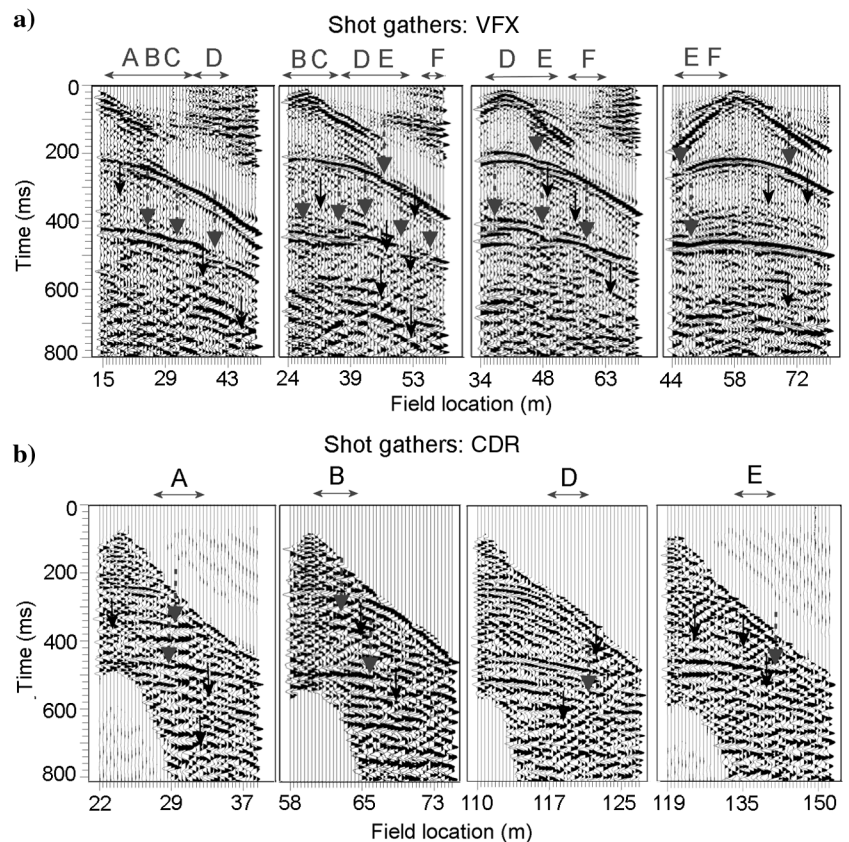


Figure 8. Representative shot gathers showing discontinuity or undulation (dashed-line arrows) in the reflection moveout in: (a) VFX data and (b) CDR data. Letters A to F mark field locations where steplike changes in HOVA and disturbances in the main reflection horizons in the stacked section were found (Figures 5 and 6). Arrows (black) with solid line show indications of backscattered arrivals. Arrows (dark gray) with dashed line mark discontinuities in reflection moveout.

tude of the undulation in the reflection moveout in Figure 9d is due to the limited width of the fault segment and no vertical displacement (throw) of layer boundaries in our model. The undulations/breaks in the reflection moveout in Figure 9d are less prominent than those noticed in the field shot gathers (Figure 8) and in more realistic, synthetic shot gathers to be illustrated later on.

We have not experimented with the dip of the disturbed zone to reproduce the exact orientation (i.e., velocity) of the backscattered energy because this was not our goal. Notice that the undulation and disturbance in the moveout of the primary reflection events (marked by arrows in Figure 9d) also resemble with what we notice in the field data (Figure 8a and 8b). Small-amplitude diffraction-like events are visible in field and synthetic shot gathers around the fault segment. Modeling with several fault segments with varying

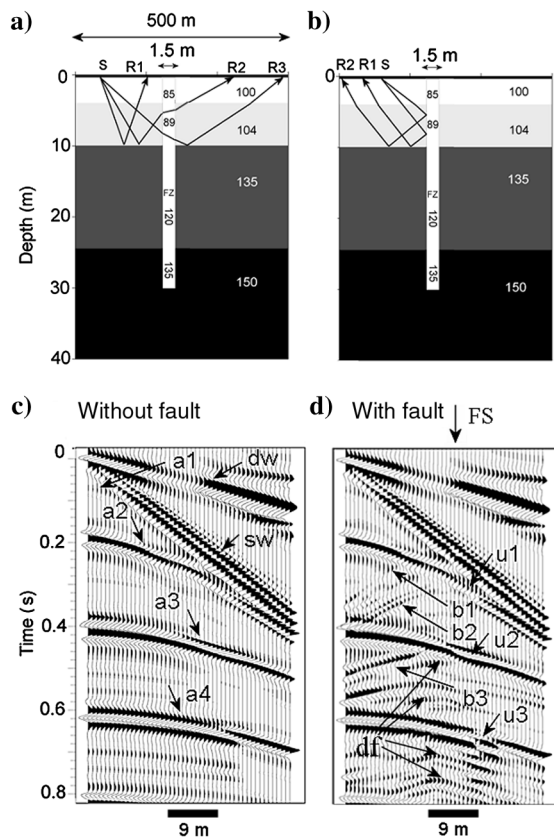


Figure 9. (a) A four-layered soil model with a vertically emplaced, local disturbed zone. The numbers indicate S-wave velocities in m/s. Reflected waves from soil layers transmitted through the disturbed zone may be recorded in receivers R1, R2, and R3. The ray bending at the low-velocity-disturbed zone will cause undulation in reflection moveout. (b) Reflected (backscattered) energy at the disturbed zone may arrive at receivers R1 and R2. (c) Synthetic shot gather for the same four-layered model as in (a and b) but without the disturbed zone; dw is direct wave; sw is the surface wave train; and a1, a2, a3, and a4 are reflections, which match well with observations in the field data (see Figure 8a). (d) Synthetic shot gather for the same model but with the disturbed zone; b1, b2, and b3 show backscattered arrivals; u1, u2, and u3 mark undulations in the reflection moveout, similar to observation in the field data (see Figure 8). Several diffracted arrivals (df) from the disturbed zone can be identified; and FS (arrow on the top margin in [d]) indicates the fault segment location.

width and velocity contrast shows that these events are indeed diffractions.

These modeling results are crucial to attach confidence to the interpreted expressions of shallow fault segments or disturbed zones in the S-wave reflection data (Figures 5–8). However, a more rigorous check should consider the presence of multiple fault segments or disturbed zones and investigate if the appearance of the different events in different shot gathers in the field data can sufficiently be explained. The evidences detected in shallow S-wave reflection data at the VFX and CDR sites are discussed in the previous section. Based on these evidences, the location, thickness, and depth of the disturbed zones in a composite 2D model are assigned. Figure 10a and 10b shows the 2D models for VFX and CDR, respectively. The thickness and depth of the disturbed zones conform with the general observations made on outcrops and trenches in the Iberian Peninsula and other comparable tectonic settings (e.g., Cabral et al., 2004; D'Amato et al., 2009; Rockwell et al., 2009). The acquisition geometry and the location of seismic source and receiver are identical between field and synthetic tests.

Figure 11a shows the field shot gathers for four different source locations along the seismic line at the VFX site (same shot gathers as in Figure 8a). The backscattered and diffracted events in these shot gathers are marked by black (continuous-line) arrows. Figure 11b shows the synthetic shots gathers with source and receivers

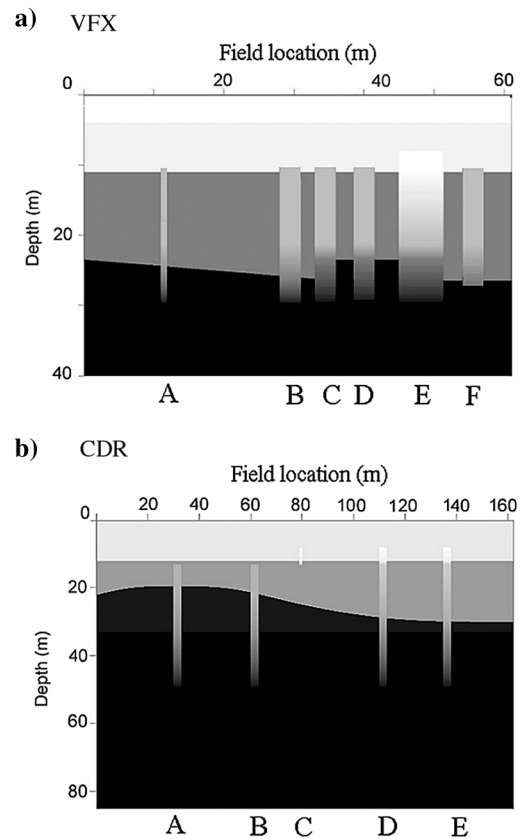


Figure 10. Model with multiple disturbed zones or fault segments at the (a) VFX site and (b) CDR site. Location and width of the disturbed zones are assigned based on observed disturbances in field S-wave reflection data (Figures 5 to 8).

located at the same positions as for the field gathers in Figure 11a, for the model containing multiple disturbed zones as shown in Figure 10a. It is evident at first sight that many of the backscattered/diffracted arrivals are positioned similarly between field and synthetic shot gathers (see continuous-line arrows in Figure 11). As mentioned earlier, we have not experimented with the dip of the disturbed zones, but nevertheless the appearance of similar scattered events in the synthetic data is striking. Note also that not only the scattered energy but the location of the discontinuities in the reflection moveout also generally matches between field and synthetic shot gathers (marked by dashed-line arrows).

Figure 12 shows the field and modeled shot gathers for the CDR site. The model shown in Figure 10b is used in synthetic seismogram generation. Here too, the source and receivers are identically located between field and synthetic tests. The field data are noisier for CDR compared to VFX. The field shot gathers are, therefore, top muted to highlight the reflections and the scattered events. We mark the backscattered arrivals (continuous-line arrows) and the discontinuities in the reflection moveout (dashed-line arrows) that resemble between field and synthetic shot gathers.

Using the modeled shot gathers, we produced synthetic stacked sections for the VFX and CDR sites, using identical processing steps as those applied to field data. The results are presented in Figure 13a and 13b, respectively. Note that the last interface of the CDR model shown in Figure 10b corresponds to the event (Refl.3) at approximately 500 ms two-way time in the field data, and there is no other interface beyond this time in our model. This explains why we do not see any reflector below Refl.3 in the modeled stacked section, unlike in the field section.

Figure 13 illustrates that the main structural features of the field stacked section are well-reproduced in the synthetic sections. This is noteworthy, considering the simplicity of the model used. Dotted ellipses in Figure 13 mark the location of features associated with the presence of the fault segments, which are visible in field and synthetic sections. Some discrepancy in the appearance of backscattered/diffracted energy between field and modeled data sets will be discussed in the "Discussion" section.

DISCUSSION

It is remarkable that with a simple model of narrow vertical segments of disturbances emplaced in horizontally lying soil layers, we could reproduce the key characteristics of the disturbances observed in the S-wave seismic wavefield.

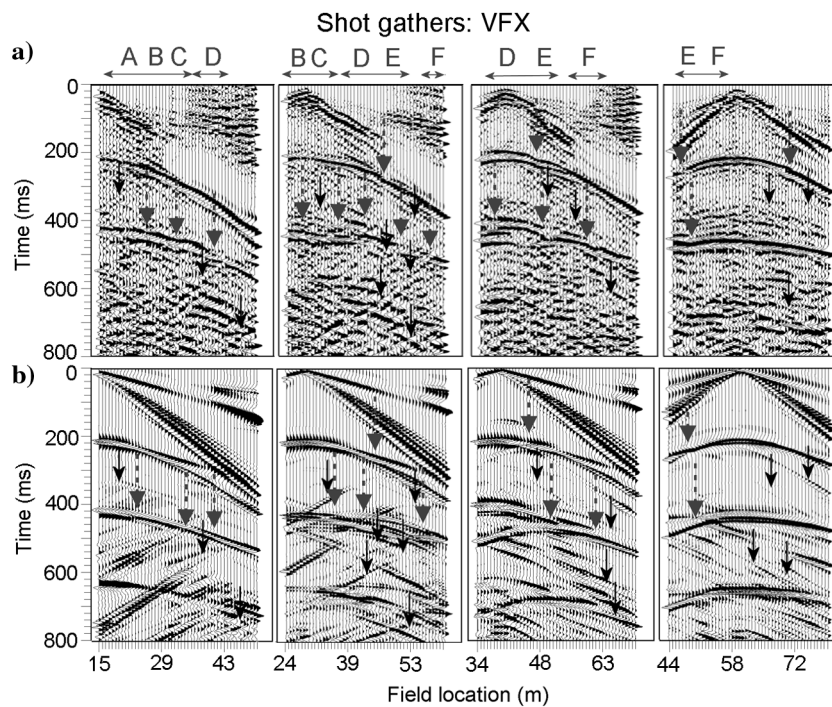


Figure 11. Observed and modeled shot gathers at VFX site: (a) Field shot gathers (same as in Figure 8b) with backscattered and diffracted energy marked by continuous-line (black) arrows and discontinuities in the main reflection moveouts shown by dashed-line (dark gray) arrows. (b) Synthetic shot gathers for a subsoil model with multiple disturbed zones as shown in Figure 10a.

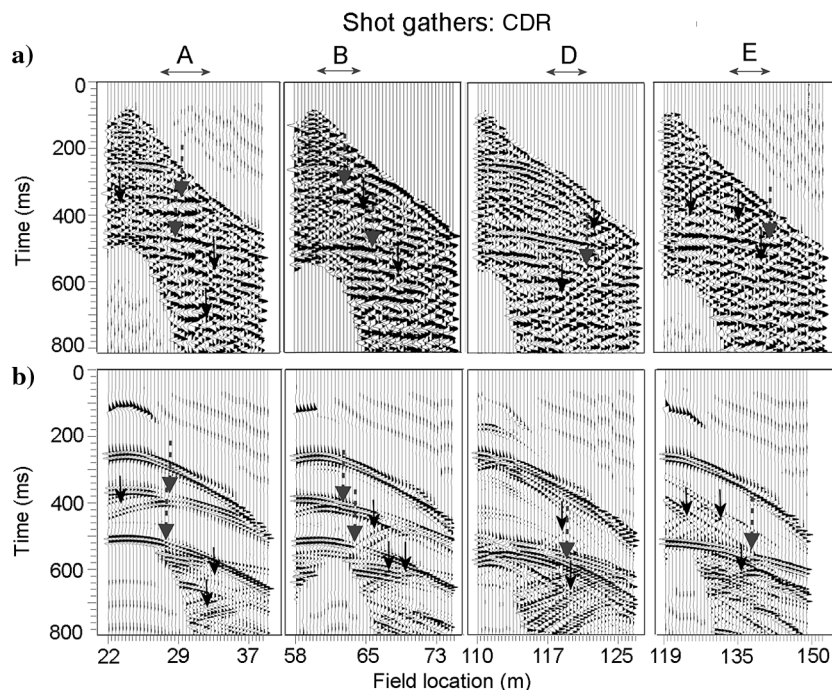


Figure 12. Observed and modeled shot gathers at CDR site: (a) Field shot gathers (same as in Figure 8b) with backscattered and diffracted energy marked by continuous-line (black) arrows and discontinuities in main reflection moveout shown by dashed-line (dark gray) arrows. (b) Synthetic shot gathers for a subsoil model with multiple disturbed zones as shown in Figure 10b.

In our model, there is no vertical discontinuity in the layer boundaries across a fault segment or a disturbed zone. There are only vertically emplaced low-velocity areas to grossly mimic the fluid-bearing zones in soil that have undergone ductile deformation due to earthquake-induced ground motion, such as those illustrated in Figure 1. These low-velocity fault segments have a constant velocity gradient with depth, to keep the velocity contrast with adjacent sediments constant. This would correspond to the field situation, as the overburden stress increases with depth. The general resemblance between the modeled and the field shot gathers is, notwithstanding, quite good. This indicates that the interpretation of the evidences of soft-sediment deformation in seismic reflection data is generally valid. Finding six different evidences, some of them being mutually related, for the presence of locally disturbed zones in soil, together with the good match between field and synthetic shot gathers, increase the confidence in interpretation.

We have checked the effect of static correction on any of the consistent features in the seismic data that we consider as an expression of damage/deformation segments in the shallow subsoil. We find that the observed conspicuous features in field data cannot be explained by near-surface effects. The sharp disturbances found in the data are also not compatible with larger-wavelength lithological

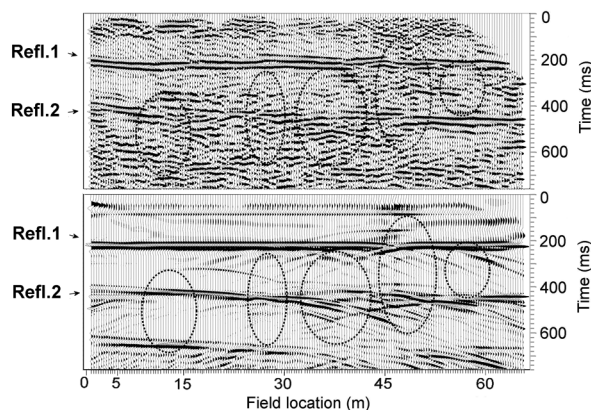
changes that are common in the alluvium in this region as found in well data, such as the presence of sand lenses that are a few meter thick and several tens of meters long. The GPR data recently acquired at a site located 1 km north of the CDR site could establish evidences of faulting in the Holocene alluvium, supporting our interpretation. All six evidences that we have shown are not mutually independent. They are all caused by local alterations in seismic velocity and/or structure. However, their simultaneous observation at a given location is especially meaningful. Some causes may contribute to all of these features, whereas others contribute to a part of them.

In our model, we have assigned 10%–20% velocity reduction in the disturbed zone compared to the surrounding. In case of faults in compacted formations or in hard rocks at greater depths, the deformation is brittle and the rock is generally heavily damaged in the shear zones. The velocity reduction in such fault zones can be as high as 50% (e.g., Kuwahara and Ito, 2002; Cochran et al., 2009). In our study area, the deformation of water-saturated, unconsolidated clayey sediments will have a plastic behavior, and the velocity reduction is expected to be much less. The velocity reduction in this case happens due to mechanisms such as intrusion of liquefied sand along weak zones, mixing, and wedgelike penetration of material with different hydromechanical properties. This type of deformation occurs in association with liquefaction, which was reported in this area during the 1909, 1858, 1755, and 1531 earthquakes (Johnston and Kanter, 1990; Mendes-Victor et al., 1994, 2009; Cabral et al., 2004). We notice indeed 10%–20% velocity reduction in the result of HOVA analysis. At a greater depth, the effect of repeated occurrence of earthquake-induced ground shaking can be responsible for a greater reduction in seismic velocity in a disturbed zone than at a shallow depth region, which has experienced relatively less number of earthquakes. Therefore, it is possible to use the detected velocity reduction as a means to evaluate the state of a damaged zone.

The interpreted width of a disturbed zone in this study is very small compared to large, regional fault zones, which may extend to several kilometers (Nielsen et al., 1998, 2005; Cochran et al., 2009). However, here, we are dealing with individual, localized damaged zones, or fault segments, which, according to previous trench data, have a typical width of 0.2–1 m (e.g., Perea et al., 2003; Ferry et al., 2005; Rockwell et al., 2009). At greater depths, cumulative slip may generate Euclidean-type geometry (planar or tabular faults, with smoothly varying properties in a continuum, Fung, 1977) for faults with a greater width (Ben-Zion and Sammis, 2003). Trench data have also shown that typical shallow faults in the intraplate low-slip-rate regions such as Portugal, Spain, the Rhine-Graben, or Mongolia have generally steeply dipping fault planes (e.g., Perea et al., 2003; Ferry et al., 2005; Rockwell et al., 2009). This supports the assumption made here.

The emplacement of multiple disturbed zones in the model based on field evidences and the good match between field and observed shot

a) S-wave stack: VFX



b) S-wave stack: CDR

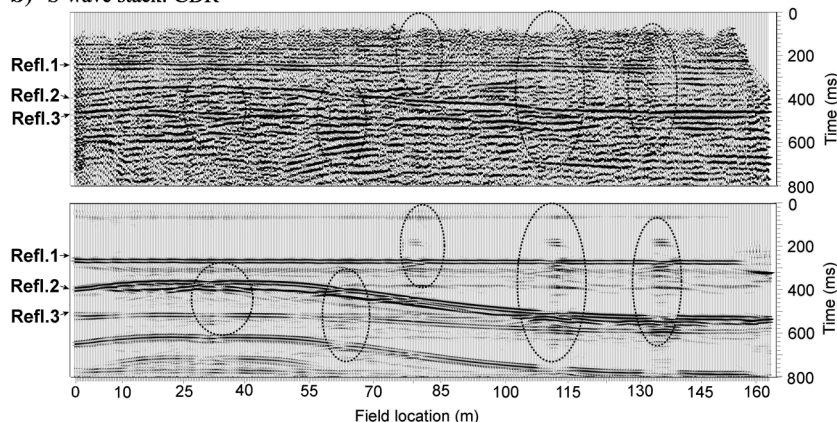


Figure 13. Field (above) and synthetic (below) unmigrated stacked sections for (a) VFX and (b) CDR sites. The models, containing multiple fault segments, which are used to produce the synthetic stacked sections are shown in Figure 10. The synthetic sections were obtained using a similar processing flow as the field data. Dotted ellipses mark areas suggesting the presence of faulting-related disturbances.

gathers at different locations is a check of the interpretation. Simple vertical disturbed zones and planar interfaces were used in the model. Not all the evidences — discontinuities in the reflection moveout, backscattered arrivals, and aligned diffractions that we see in the synthetic data are equally clear in field data. We have marked only a few that are evident and that can explain that these features can be produced in the seismic wavefield in case earthquake-shaking-induced disturbed zones are present, hidden in the shallow subsoil. Because a full inversion of the recorded wavefield is not performed to obtain the subsurface model, our forward model, by no means, presents a complete/accurate picture of the subsurface. Not all scattered events present in the synthetic shot gathers and stacked section are present in the field shot gathers and the stacked sections, and vice versa. This is due to the complexity of real fault branching that is not addressed in the simple modeling carried out here. The train of dispersive surface waves at VFX has a greater amplitude in synthetic data than in field data. The single value for seismic attenuation that we assumed for the whole model space does not represent the relatively compacted top soil layer at this site.

As stated earlier, in this research, we attempted detection of fault segments (branches) with minimal throws and shaking-induced ductile deformation in soft soil, such as intruded materials from below, which are at the limit of temporal seismic resolution (approximately 0.5 m in our data). The results presented here show that the velocity field contains information with resolution exceeding that in the stacked section, as also reported earlier (Ghose and Goudswaard, 2004).

Detecting the evidence of soft-sediment deformation in the shallow seismic reflection data is a challenging task, especially when the deformation is highly localized. The approach presented in this paper offers a possibility to meet this challenge. As a next step, one can consider performing an inversion, minimizing the difference between field and synthetic data sets to obtain more accurate values for the dip and the location of the disturbed zones.

CONCLUSIONS

Compared to the detection of faulting-induced major displacements of geologic boundaries, the detection of ductile, soft-sediment deformation, or damaged zones in soil due to earthquake-induced ground shaking is more difficult in the shallow seismic reflection data. This is primarily because the soft-sediment deformations generally do not create a sharp lateral change in a geologic boundary, but they rather result in localized grain reorganization, material mixing, and subtle fluid-flow-induced structures. A priori detection of seismogenic disturbed zones hidden in soil cover is important for probabilistic evaluation of earthquake occurrences, in seismic site characterization studies, and for hydrogeologic and engineering considerations.

We found that, for recognizing and interpreting the presence of such disturbances in the shallow seismic reflection data, identification of multiple evidences in the data and confirmation of them through simple but careful forward modeling lead to an effective and reliable exploration approach. The use of S-waves in the unconsolidated soil is advantageous not only because of the high resolution due to the low velocity of S-waves in soft soils, but also because of the high sensitivity of S-waves to subtle changes in the soil. Lateral variation of V_S can be a key diagnostic in identifying earthquake-motion-induced disturbed zones in the shallow subsoil.

We found six different evidences of soft-sediment deformation in the shallow S-wave reflection data at VFX and CDR sites in Por-

tugal. These evidences are (1) local changes in the semblance velocity determined by automatic HOVA of the primary reflection events, (2) disturbances or discontinuities in the primary reflection horizons in the stacked section, (3) aligned diffractions identified in the unmigrated stacked sections, (4) pronounced discontinuity or undulation in the main reflectors in the COG, (5) discontinuity or undulation in reflection moveout in common-source or shot gathers, and (6) prominent backscattered arrivals and diffractions from the fault segment or the disturbed zone visible in the shot gathers. Although all of these six evidences do not manifest equally clearly at every location, they are all recognizable at each location where earthquake-motion-induced disturbances are interpreted.

To verify these interpretations, we have performed forward modeling and have compared those evidences between field shot gathers and synthetic shot gathers. In synthetic modeling, the parameters were the same as in field seismic acquisition. Multiple disturbed zones at different locations in each site, as interpreted in S-wave seismic reflection data, are included in the model. In the disturbed zones in model, the assigned S-wave velocity is 10%–20% less than the background velocity, as found in the semblance velocity analysis. It is remarkable that with this simple model consisting of localized disturbed zones or fault segments (as interpreted in field data) vertically emplaced in horizontally lying soil layers, we can reproduce the main observed features in the seismic shot gathers. The good match between observed and modeled shot gathers at different locations and between real-data and synthetic stacked sections supports the interpretation.

The approach presented here, involving use of S-waves, identification of multiple evidences in the shallow seismic reflection data, and further appraisal through realistic forward modeling, should be useful in different seismically active, soil-covered areas in the world.

ACKNOWLEDGMENTS

The authors are grateful to the Portuguese Foundation for Science and Technology for financing projects ATESTA-PTDC/CTE-GIX/099548/2008 and SISMOD/LISMOT-PTDC/CTE-GIN/82704/2006, under which seismic data were acquired. B. Caldeira and J. Borges, principal investigators of these projects, are acknowledged. The assistance of C. Pinto and F. Caneiras in the field is greatly appreciated. We would like to thank associate editors S. Hanafy and J. Zaskie, and E. Skomedal and two anonymous reviewers for their comments, which helped improving the clarity of this manuscript. We are grateful to J. Palha and J. Lopes, the landowners of the VFX and CDR sites, respectively, for their permission.

REFERENCES

- Alsop, G. I., and S. Marco, 2011, Soft-sediment deformation within seismogenic slumps of the Dead Sea Basin: *Journal of Structural Geology*, **33**, 433–457, doi: [10.1016/j.jsg.2011.02.003](https://doi.org/10.1016/j.jsg.2011.02.003).
- Bensaúde, A., D. Fonseca, G. Rodríguez, J. M. Miranda, L. Senos, M. A. Baptista, M. Solares, M. Victor, M. Rodríguez, P. Choffat, P. de Sousa, P. de la Torre, S. Moreira, S. Oliveira, S. Vilanova, and T.-E. Cherkaoui, 2011, Killer earthquakes in Portugal (mainland), <http://earthquake-report.com/2011/02/07/killer-earthquakes-in-portugal-mainland/>, accessed 15 June 2016.
- Benson, A. K., and N. B. Mustoe, 1995, Analyzing shallow faulting at a site in the Wasatch fault zone, Utah, USA, by integrating seismic, gravity, magnetic, and trench data: *Engineering Geology*, **40**, 139–156, doi: [10.1016/0013-7952\(95\)00060-7](https://doi.org/10.1016/0013-7952(95)00060-7).
- Ben-Zion, Y., and C. G. Sammis, 2003, Characterization of fault zones: *Pure and Applied Geophysics*, **160**, 677–715, doi: [10.1007/PL00012554](https://doi.org/10.1007/PL00012554).
- Bray, J. D., R. B. Seed, L. S. Cluff, and H. B. Seed, 1994, Earthquake fault rupture propagation through soil: *Journal of Geotechnical Engineering*, **120**, 543–561, doi: [10.1061/\(ASCE\)0733-9410\(1994\)120:3\(543\)](https://doi.org/10.1061/(ASCE)0733-9410(1994)120:3(543)).

- Brouwer, J., R. Ghose, K. Helbig, and V. Nijhof, 1997, The improvement of geotechnical subsurface models through the application of S-wave reflection seismic exploration: Proceedings of Engineering and Environmental Geophysics European Section Meeting, 103–106.
- Campbell, F. M., F. Ghisetti, A. E. Kaiser, A. G. Green, H. Horstmeyer, and A. R. Gorman, 2010, Structure and evolution of the seismically active Ostler Fault Zone (New Zealand) based on interpretations of multiple high resolution seismic reflection profiles: *Tectonophysics*, **495**, 195–212, doi: [10.1016/j.tecto.2010.09.016](https://doi.org/10.1016/j.tecto.2010.09.016).
- Cabral, J., C. Moniz, J. Batló, P. Figueiredo, J. Carvalho, L. Matias, P. Teves-Costa, R. Dias, and N. Simão, 2013, The 1909 Benavente (Portugal) earthquake: Search for the source: *Natural Hazards*, **69**, 1211–1227, doi: [10.1007/s11069-011-0062-8](https://doi.org/10.1007/s11069-011-0062-8).
- Cabral, J., C. Moniz, P. Ribeiro, P. Terrinha, and L. Matias, 2003, Analysis of seismic reflection data as a toll for the seismotectonic assessment of the low activity intraplate basin — The Lower Tagus Valley (Portugal): *Journal of Seismology*, **7**, 431–447, doi: [10.1023/B:JOSE.0000005722.23106.8d](https://doi.org/10.1023/B:JOSE.0000005722.23106.8d).
- Cabral, J., P. Ribeiro, P. Figueiredo, N. Pimentel, and A. Martins, 2004, The Azambuja fault: An active structure located in an intraplate basin with significant seismicity (Lower Tagus Valley, Portugal): *Journal of Seismology*, **8**, 347–362, doi: [10.1023/B:JOSE.0000038450.23032.68](https://doi.org/10.1023/B:JOSE.0000038450.23032.68).
- Campbell, F. M., F. Ghisetti, A. E. Kaiser, A. G. Green, H. Horstmeyer, and A. R. Gorman, 2010, Structure and evolution of the seismically active Ostler Fault Zone (New Zealand) based on interpretations of multiple high resolution seismic reflection profiles: *Tectonophysics*, **495**, 195–212, doi: [10.1016/j.tecto.2010.09.016](https://doi.org/10.1016/j.tecto.2010.09.016).
- Carvalho, J., J. Cabral, R. Gonçalves, L. Torres, and L. Mendes-Victor, 2006, Geophysical methods applied to fault characterization and earthquake potential assessment in the Lower Tagus Valley, Portugal: *Tectonophysics*, **418**, 277–297, doi: [10.1016/j.tecto.2006.02.010](https://doi.org/10.1016/j.tecto.2006.02.010).
- Carvalho, J., H. Matias, L. Torres, G. Manupella, R. Pereira, and L. Mendes-Victor, 2005, The structural and sedimentary evolution of the Arruda and Lower Tagus sub-basins, Portugal: *Marine and Petroleum Geology*, **22**, 427–453, doi: [10.1016/j.marpetgeo.2004.11.004](https://doi.org/10.1016/j.marpetgeo.2004.11.004).
- Carvalho, J., T. Rabeh, F. Carrilho, J. Cabral, and M. Miranda, 2008, Geophysical characterization of the Ota-Vila Franca de Xira-Lisbon-Sesimbra fault zone, Portugal: *Geophysical Journal International*, **174**, 567–584, doi: [10.1111/gji.2008.174.issue-2](https://doi.org/10.1111/gji.2008.174.issue-2).
- Carvalho, J., P. Sousa, J. Matos, and C. Pinto, 2011, Ore prospecting in the Iberian Pyrite Belt using seismic and potential-field data: *Journal of Geophysics and Engineering*, **8**, 2, 142–153.
- Chester, F. M., C. Rowe, K. Ujiie, J. Kirkpatrick, C. Regalla, F. Remitti, J. C. Moore, V. Toy, M. Wolfson-Schwehr, S. Bise, J. Kameda, J. J. Mori, E. E. Brodsky, N. Eguchi, and S. Toczko, 2013, Structure and composition of the plate-boundary slip zone for the 2011 Tohoku-Oki earthquake: *Science*, **342**, 1208–1211, doi: [10.1126/science.1243719](https://doi.org/10.1126/science.1243719).
- Cochran, E. S., Y.-G., Li, P. M. Shearer, S. Barbot, Y. Fialko, and J. E. Vidale, 2009, Seismic and geodetic evidence for extensive, long-lived fault damage zones: *Geology*, **37**, 315–318, doi: [10.1130/G25306A.1](https://doi.org/10.1130/G25306A.1).
- D'Amato, D., B. Pace, J. Cabral, and P. M. Figueiredo, 2009, The Vale de Santarém Neogene trough in the seismotectonics framework of the Lower Tagus Valley (Portugal): *Trabajos de Geología, Universidad de Oviedo*, **29**, 200–205.
- Ferry, M., M. Meghraoui, B. Delouis, and D. Giardini, 2005, Evidence for Holocene paleoseismicity along the Basel-Rheinach active normal fault (Switzerland): A seismic source for the 1356 earthquake in the Upper Rhine Graben: *Geophysical Journal International*, **160**, 554–572, doi: [10.1111/gji.2005.160.issue-2](https://doi.org/10.1111/gji.2005.160.issue-2).
- Floyd, J. S., J. C. Mutter, A. M. Goodlife, and B. Taylor, 2001, Evidence of fault weakness and fluid flow within an active low-angle normal fault: *Nature*, **411**, 779–783, doi: [10.1038/35081040](https://doi.org/10.1038/35081040).
- Fossen, H., 2010, Deformation bands formed during soft-sediment deformation: Observations from SE Utah: *Marine and Petroleum Geology*, **27**, 215–222, doi: [10.1016/j.marpetgeo.2009.06.005](https://doi.org/10.1016/j.marpetgeo.2009.06.005).
- Fung, Y. C., 1977, *A first course in continuum mechanics* (2nd ed.): Prentice-Hall Inc.
- Ghose, R., 2003, High-frequency shear-wave reflections to monitor lateral variations in soil, supplementing downhole geotechnical tests, in J. Saveur, ed., *Reclaiming the underground space*: Swets & Zeitlinger, 827–833.
- Ghose, R., 2012, A microelectromechanical system digital 3C array seismic cone penetrometer: *Geophysics*, **77**, no. 3, WA99–WA107, doi: [10.1190/geo2011-0266.1](https://doi.org/10.1190/geo2011-0266.1).
- Ghose, R., J. Carvalho, and A. Loureiro, 2013, Signature of fault zone deformation in near-surface soil visible in shear-wave seismic reflections: *Geophysical Research Letters*, **40**, 1074–1078, doi: [10.1002/grl.50241](https://doi.org/10.1002/grl.50241).
- Ghose, R., and J. Goudswaard, 2004, Integrating S-wave seismic reflection data and cone-penetration-test data using a multiangle multiscale approach: *Geophysics*, **69**, 440–459, doi: [10.1190/1.1707064](https://doi.org/10.1190/1.1707064).
- Hale, D., 1984, Dip-moveout by Fourier transform: *Geophysics*, **49**, 741–757, doi: [10.1190/1.1441702](https://doi.org/10.1190/1.1441702).
- Harris, J. B., 2009, Hammer-impact SH-wave seismic reflection methods in neotectonic investigations: General observations and case histories from the Mississippi embayment, U.S.A.: *Journal of Earth Science*, **20**, 513–525, doi: [10.1007/s12583-009-0043-y](https://doi.org/10.1007/s12583-009-0043-y).
- Jiménez-Munt, I., and A. M. Negrodo, 2003, Neotectonic modelling of the western part of the Africa-Eurasia plate boundary: From the Mid-Atlantic ridge to Algeria: *Earth and Planetary Science Letters*, **205**, 257–271, doi: [10.1016/S0012-821X\(02\)01045-2](https://doi.org/10.1016/S0012-821X(02)01045-2).
- Johnston, A. C., and L. R. Kanter, Earthquakes in stable continental crust: *Scientific American*, **262**, 68–75, 1990, doi: [10.1038/scientificamerican.0390-68](https://doi.org/10.1038/scientificamerican.0390-68).
- Justo, J. L., and C. Salwa, 1998, The 1531 Lisbon earthquake: *Bulletin of the Seismological Society of America*, **88**, 319–328.
- Kuwahara, Y., and H. Ito, 2002, Fault low velocity zones deduced by trapped waves and their relation to earthquake rupture processes: *Earth Planets Space*, **54**, 1045–1048, doi: [10.1186/BF03353299](https://doi.org/10.1186/BF03353299).
- Mendes-Victor, L. A., C. S. Oliveira, J. Azevedo, and A. Ribeiro, eds., 2009, *The 1755 Lisbon earthquake revisited*: Springer.
- Mendes-Victor, L. A., C. S. Oliveira, I. Pais, and P. Teves-Costa, 1994, Earthquake damage scenarios in Lisbon for disaster preparedness, in B. E. Tucker, M. Erdik, and C. N. Hwang, eds., *Issues in urban risk*: Springer, 271, NATO ASI Series, 265–289.
- Neuwerth, R., F. Suter, C. A. Guzman, and G. E. Gorin, 2006, Soft-sediment deformation in a tectonically active area: The Plio-Pleistocene Zarzal Formation in the Cauca Valley (Western Colombia): *Sedimentary Geology*, **186**, 67–88, doi: [10.1016/j.sedgeo.2005.10.009](https://doi.org/10.1016/j.sedgeo.2005.10.009).
- Nielsen, L., H. Thybo, and M. I. Jørgensen, 2005, Integrated seismic interpretation of the Carlsberg Fault zone, Copenhagen, Denmark: *Geophysical Journal International*, **162**, 461–478, doi: [10.1111/j.1365-246X.2005.02664.x](https://doi.org/10.1111/j.1365-246X.2005.02664.x).
- Nielsen, L., H. Thybo, T. Klinkby, and N. Balling, 1998, Fault detection from back-scattered energy in MONA LISA wide-angle seismic sections from the south-eastern North Sea: *First Break*, **16**, 119–126, doi: [10.1046/j.1365-2397.1998.00688.x](https://doi.org/10.1046/j.1365-2397.1998.00688.x).
- Perea, H., P. Figueiredo, J. Carner, S. Gambini, and K. Boydell, 2003, Paleoseismological data from a new trench across the El Camp Fault (Catalan Coastal Ranges, NE Iberian Peninsula): *Annals of Geophysics*, **46**, 763–774.
- Pisarska-Jamro, M., and P. Weckwerth, 2013, Soft-sediment deformation structures in a Pleistocene glaciolacustrine delta and their implications for the recognition of subenvironments in delta deposits: *Sedimentology*, **60**, 637–665, doi: [10.1111/j.1365-3091.2012.01354.x](https://doi.org/10.1111/j.1365-3091.2012.01354.x).
- Rasmussen, E. S., S. Lomholt, C. Anderson, and O. V. Vejbæk, 1998, Aspects of the structural evolution of the Lusitanian Basin in Portugal and the shelf and slope area offshore Portugal: *Tectonophysics*, **300**, 199–225, doi: [10.1016/S0040-1951\(98\)00241-8](https://doi.org/10.1016/S0040-1951(98)00241-8).
- Rockwell, T., J. Fonseca, C. Madden, T. Dawson, L. A. Owe, S. Vilanova, and P. Figueiredo, 2009, Paleoseismology of the Vilaria segment of the Manteigas-Bragana fault in northeastern Portugal, in K. Reicherter, A. M. Michetti, and P. G. Silva, eds., *Paleoseismology: Historical and pre-historical records of earthquake ground effects for seismic hazard assessment*: The Geological Society, London, Special Publications **316**, 237–258.
- Stolt, R. H., 1978, Migration by Fourier transform: *Geophysics*, **43**, 23–48, doi: [10.1190/1.1440826](https://doi.org/10.1190/1.1440826).
- Sugiyama, Y., K. Mizuno, F. Nanayama, T. Sugai, H. Yokota, T. Hosoya, K. Miura, K. Takemura, and N. Kitada, 2003, Study of blind thrust faults underlying Tokyo and Osaka urban areas using a combination of high-resolution seismic reflection profiling and continuous coring: *Annals of Geophysics*, **46**, 1071–1085, doi: [10.4401/ag-3446](https://doi.org/10.4401/ag-3446).
- Suter, F., J. I. Martínez, and M. I. Vélez, 2011, Holocene soft-sediment deformation of the Santa Fe–Sopetrán Basin, northern Colombian Andes: Evidence for pre-Hispanic seismic activity? *Sedimentary Geology*, **235**, 188–199, doi: [10.1016/j.sedgeo.2010.09.018](https://doi.org/10.1016/j.sedgeo.2010.09.018).
- Thorbecke, J., and D. Dragannov, 2011, Finite-difference modeling experiments for seismic interferometry: *Geophysics*, **76**, no. 6, H1–H18, doi: [10.1190/geo2010-0039.1](https://doi.org/10.1190/geo2010-0039.1).
- Vanneste, K., M. Meghraoui, and T. Camelbeck, 1999, Late Quaternary earthquake-related soft-sediment deformation along the Belgian portion of the Feldbiss Fault, Lower Rhine Graben system: *Tectonophysics*, **309**, 57–79, doi: [10.1016/S0040-1951\(99\)00132-8](https://doi.org/10.1016/S0040-1951(99)00132-8).
- van Loon, A. J., 2009, Soft-sediment deformation structures in siliciclastic sediments: An overview: *Geologos*, **15**, 3–55.
- Vis, G., and C. Kasse, 2009, Late Quaternary valley-fill succession of the Lower Tagus Valley, Portugal: *Sedimentary Geology*, **221**, 19–39, doi: [10.1016/j.sedgeo.2009.07.010](https://doi.org/10.1016/j.sedgeo.2009.07.010).
- Wang, Z., I. P. Madlin, and E. W. Woolery, 2004, Shallow SH-wave seismic investigation of the Mt. Angel Fault, Northwest Oregon, USA: *Tectonophysics*, **368**, 105–117, doi: [10.1016/S0040-1951\(03\)00153-7](https://doi.org/10.1016/S0040-1951(03)00153-7).
- Williams, R. A., W. J. Stephenson, J. K. Odum, and D. M. Worley, 2001, Seismic reflection imaging of Tertiary faulting and related post-Eocene deformation 20 km north of Memphis, Tennessee: *Engineering Geology*, **62**, 79–90, doi: [10.1016/S0013-7952\(01\)00052-7](https://doi.org/10.1016/S0013-7952(01)00052-7).
- Woolery, E. W., R. Street, Z. Wang, and J. B. Harris, 1993, Near surface deformation in the New Madrid seismic zone as imaged by high-resolution SH-wave seismic methods: *Geophysical Research Letters*, **20**, 1615–1618, doi: [10.1029/93GL01658](https://doi.org/10.1029/93GL01658).